MASTER'S THESIS

Sensor Design for Characterization of Metallic Nanoparticles

Álvaro Martín Martín

Directors: Romano Giannetti and Francisco Javier Herraiz Martínez

Abstract

This paper addresses the growing need for rapid, in-line characterization of metallic nanoparticles by demonstrating a compact metamaterial-based sensor for nanoparticle characterization. We employ a microwave-frequency resonator whose response shifts measurably when local material properties change. Copper and iron nanoparticles (synthesized via a controlled wire-explosion method) are suspended in a liquid medium and introduced over the sensor's surface. As the particles settle under gravity, they alter the effective electrical properties immediately above the resonator, producing a time-dependent shift in its resonant frequency. By continuously recording these shifts with a Vector Network Analyzer (VNA), we obtain detailed frequency-versus-time curves that capture both the sedimentation kinetics and the overall magnitude of the resonance peaks. An inversion algorithm is then applied to fit these curves with multi-exponential functions, yielding characteristic sedimentation time constants for each sample. The results demonstrate clear differentiation between copper and iron nanoparticle dispersions, and even discriminate between samples of the same material that have different size distributions. By combining metamaterial resonance with data-driven analysis, this work establishes a non-destructive, optics-free methodology for real-time nanoparticle analytics. Its compact form factor and minimal sample preparation make it well suited for integration into flow-through industrial process lines. The findings lay the groundwork for future enhancements, including sensor arrays for multiplexed measurements, extension to other nanomaterials, and closed-loop control systems for autonomous process monitoring and optimization.

Keywords: metallic nanoparticles, industry 4.0, metamaterial, microwave resonator, sedimentation, time constant extraction, real-time sensing, dispersion

1. Introduction

Nanotechnology refers to the branch of science and engineering which studies structures less than 100 nanometers in length. Nanotechnology has many revolutionary applications in fields such as electronics, biotechnology and medicine[25]. Particles ranging from 1 nm to 100 nm are usually referred to as nanoparticles (NPs). These powders show easy bonding with the contact materials, have a large surface area, low melting point and peculiar electromagnetic and optical characteristics [19].

Characterizing nanoparticles is the first step to guaranteeing they behave the way they should. Evaluating the outcome of the production processes is important in order to readjust the production parameters to obtain the desired output in a closed loop. Measuring some properties, including particle size, size distribution, surface charge, or shape is generally not an easy task [24]. Key size parameters are commonly obtained using microscopy techniques, mainly Scanning Electron Microscopy (SEM) and Transmission Electron Microscopy (TEM). These methods are used alongside visual measurements, since they output images of the particles, enabling the assessment of dimensional distributions.

These characterization methods often require a time consuming process with complex instrumentation and many manual interventions, causing huge delays in the fabrication process and verification of the experiments while being quite expensive. The development of new, faster and cheaper fabrication processes is key in the development and integration of nanotechnology and nanoparticles into industrial processes [19].

1.1 Nano-particles: What are they?

Due to their unique properties, nanoparticles and nanomaterials are used in a variety of applications, ranging from water treatment, medicine, agriculture, to energy storage [5]. There are two main factors that lead to the different behaviour of NPs in contrast to the same materials at larger dimensions: surface effects and quantum effects. These factors make nanomaterials exhibit enhanced or novel mechanical, thermal, magnetic, electronic, optical and catalytic properties [29].

Nanomaterials have different surface effects compared to the bulk materials mainly due to their high surface area to mass ratio and the number of direct neighbours of surface atoms [29]. As a consequence of this, nanomaterial properties change regarding their bulk counterpart.

1.1.1 Nanomaterial Classification

Based on Dimensional Characteristics

1. Zero-dimensional (0D) nanomaterials: All three spatial dimensions are confined to the nanoscale. These materials are essentially nanoscale in every direction. Common examples include quantum dots, fullerenes, and spherical nanoparticles.
2. One-dimensional (1D) nanomaterials: These materials have two dimensions within the nanoscale, while the third extends beyond it. They typically have a high aspect ratio and are elongated in one direction. Examples include nanowires, nanotubes, nanorods, nanofibers, and nanohorns.
3. Two-dimensional (2D) nanomaterials: In this group, only one dimension remains at the nanoscale, while the other two dimensions are larger. These materials often appear

as thin films or sheets and include structures like graphene layers, nanosheets, nanofilms, and nanolayers.
4. Three-dimensional (3D) nanomaterials or bulk nanostructured materials: These materials are not restricted to the nanoscale in any of their dimensions. However, they still contain nanoscale features within their overall structure. This category includes bulk powders, nanocomposites, dispersed nanoparticle systems, and assemblies of nanowires or nanotubes.

Composition Based Classification

1. Organic Nanoparticles: Organic nanoparticles (NPs) are composed of organic compounds such as proteins, carbohydrates, lipids, and polymers [27]. Common examples include dendrimers, liposomes, micelles, and protein complexes like ferritin. These NPs are typically biodegradable, non-toxic, and, in some cases, such as liposomes, may have a hollow core. Their functionality depends on factors such as composition, surface morphology, and stability. Currently, organic NPs are widely used in biomedicine, especially for targeted drug delivery [11] and cancer therapy.
2. Carbon-based Nanoparticles: This class includes nanoparticles composed exclusively of carbon atoms [11]. Notable examples are fullerenes, carbon black, and carbon quantum dots. Carbon-based NPs are applied in fields like drug delivery, energy storage, bioimaging, photovoltaics, and environmental sensing. More complex carbon forms such as nanodiamonds and carbon nano-onions also show promise, particularly due to their low toxicity and high biocompatibility, making them suitable for drug delivery and tissue engineering[22].
3. Inorganic Nanoparticles: Inorganic NPs are those not derived from carbon-based or organic sources. They include metal, semiconductor, and ceramic nanoparticles. Metal NPs, which can be monometallic, bimetallic, or polymetallic, exhibit unique optical, thermal, electrical, and magnetic properties due to phenomena like localized surface plasmon resonance [35]. Their synthesis can be finely tuned to control size, shape, and surface characteristics, which is crucial for advanced technological applications [10]. Semiconductor NPs, made from materials with intermediate conductivity, show tunable bandgap properties that differ significantly from their bulk forms. This makes them valuable in photocatalysis and optoelectronic devices. Ceramic NPs, composed of inorganic compounds such as oxides, carbides, and phosphates, are usually formed through high-temperature processes. Found in various structural forms, they are notable for their high stability and loading capacity, making them useful in both medical applications and industrial areas like catalysis, dye degradation, and photonics [22].

1.2 Nanoparticle Production Methods

1.2.1 Top-Down Approaches

Top-down methods begin with bulk materials, reducing them to nano-scale dimensions through physical or mechanical processes. Relevant techniques within this approach include mechanical milling, laser ablation and wire explosion.

1. Mechanical milling involves the grinding of bulk materials in high-energy ball mills, where particle size is reduced through repeated impact and abrasion. This method is widely used for large-scale production due to its cost-effectiveness and ability to yield high-purity particles. However, mechanical milling poses challenges such as potential contamination from the milling media and often requires extended processing to achieve smaller particle sizes [21].
2. Laser ablation is useful for generating highly pure particles with narrow size distributions. This technique is particularly advantageous for generating highly pure particles with narrow size distributions. Nonetheless, laser ablation is energy-intensive and may experience reduced efficiency over time as particles accumulate and obstruct the laser path [21].
3. Wire Explosion (WE), which consists of a metal wire undergoing explosive fragmentation when subjected to a high-current pulse, presents unique benefits for NP synthesis. During the WE process, the wire material is rapidly ejected in the form of metal droplets and vapour, forming NPs in a surrounding medium. This method proves particularly efficient and environmentally favourable, especially in underwater applications, where energy loss is minimized as water prevents plasma formation along the wire surface and efficiently transfers the electrical energy to the wire for disintegration. While challenging to characterize due to broad and multi-modal size distributions, WE is highly reproducible for specific applications requiring stable, high-quality NPs [12].

1.2.2 Bottom-Up Approaches

In contrast to top-down methods, bottom-up approaches synthesize nanoparticles from atomic or molecular precursors, assembling them into nanoscale structures. Bottom-up methods include chemical reduction, sol-gel synthesis, and chemical vapour deposition (CVD), each offering advantages for applications requiring specific particle shapes or material compositions.

1. Chemical reduction is a widely employed technique in which metal ions are reduced in a solution to yield NPs. This method offers substantial control over particle size and shape and is a relatively low-cost option. However, chemical reduction requires stabilized agents, which may introduce contaminants. It is frequently used to synthesize gold and silver NPs, particularly in biomedical applications where particle stability and uniformity are essential [21].
2. Chemical vapour deposition (CVD) involves vaporizing metal precursors and depositing them onto a substrate,

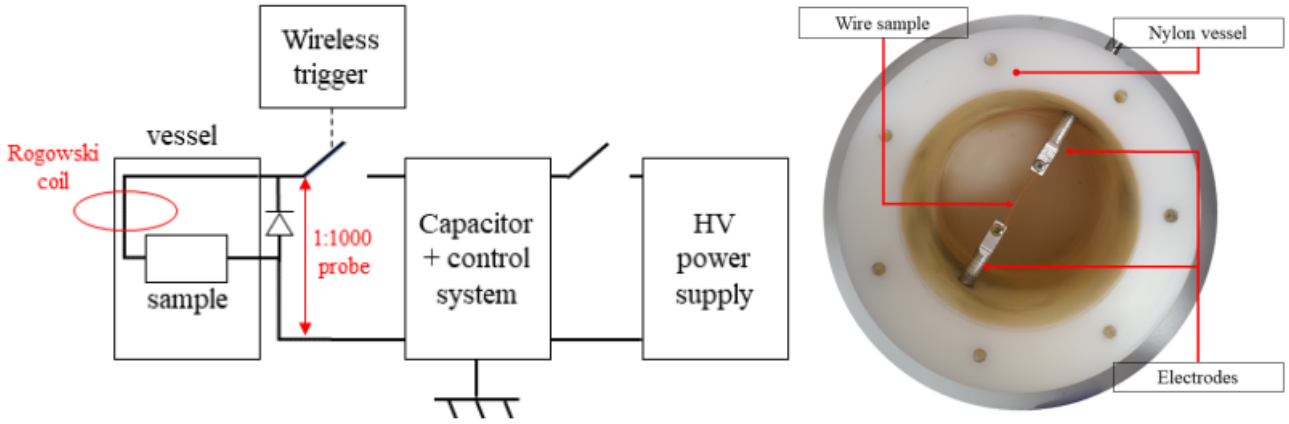

Figure 1. To the left, circuit for the wire-explosion fabrication process. To the right, vessel with a loaded wire sample used for the wire-explosion fabrication process.

where they decompose to form NPs. This technique is extensively applied in electronics and solar cells, as it produces high-purity NPs with controlled morphology. While CVD is scalable and effective for high-purity NP production, it requires expensive equipment and poses hazards due to the use of toxic precursors and high operating temperatures [15].

1.3 Nanoparticle Characterization and Classification Techniques

Nanoparticle characterization is critical to understanding the physicochemical properties that dictate functionality in applications ranging from catalysis to biomedicine. Metallic nanoparticles (MNPs), in particular gold, silver, and platinum nanosystems, exhibit size-, shape-, and composition-dependent optical, electronic, and catalytic behaviours [7, 2].

However, a comprehensive characterization strategy often requires combining multiple techniques to capture complementary information on morphology, size distribution, surface chemistry, and crystallinity [4].

1.3.1 Imaging Techniques

Transmission Electron Microscopy (TEM) TEM provides high-resolution images (< 0.1 nm) by transmitting an electron beam through an ultrathin sample [36]. Sample preparation involves drop-casting a dilute nanoparticle suspension on a carbon-coated copper grid, followed by solvent evaporation.

Contrast arises from differences in electron scattering cross-sections, allowing direct visualization of shape anisotropy in crystalline MNPs [36]. However, TEM suffers from limited statistical sampling (tens to hundreds of particles per image) and potential beam-induced damage in sensitive materials. Capital cost for a modern field-emission TEM is in the range of 800 000 € to 1 500 000 €, with annual maintenance and operation costs around 50 000 € to 100 000 € [14].

Scanning Electron Microscopy (SEM) SEM images surface topography by scanning a focused electron beam and detecting secondary electrons. While resolution (∼ 1 nm to 5 nm) is lower than TEM, SEM excels at bulk imaging over larger fields of view (tens of microns) and 3D-like contrast [16]. Conductive coating or low-voltage operation is necessary to mitigate charging in non-metallic nanoparticles.

Modern field-emission SEM instruments cost approximately 300 000 € to 600 000 €, with annual operating costs around 30 000 € [16]. SEM cannot directly resolve internal crystallinity or lattice defects.

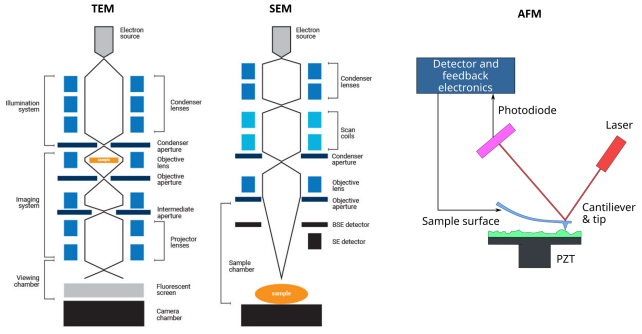

Figure 2. Imaging Techniques.

1.3.2 Spectroscopic and Scattering Techniques

Dynamic Light Scattering (DLS) DLS measures the temporal fluctuations of scattered light intensity due to Brownian motion, yielding hydrodynamic diameter distributions [4]. It provides ensemble-averaged size with high throughput (measurements in minutes) but assumes spherical geometry and is sensitive to aggregates and polydispersity [4]. DLS instruments range from 30 000 € to 70 000 €, with minimal consumables.

UV–Visible Spectroscopy Localized surface plasmon resonance (LSPR) peaks of metallic nanoparticles produce size- and composition-dependent absorption bands (e.g., gold NPs at ∼ 520 nm) [17]. UV–Vis spectrophotometers (10 000 € to

30 000 €) offer rapid, non-destructive assays, but spectral deconvolution is required for polydisperse or complex mixtures. Organic and dielectric NPs lack plasmonic signals and thus require complementary methods.

X-ray Diffraction (XRD) XRD analyzes crystalline structure by measuring Bragg diffraction of X-rays from lattice planes. Scherrer analysis provides average crystallite size, while phase identification confirms composition [6]. XRD is ensemble-based (mg-scale samples), with capital costs around 150 000 € to 300 000 € and operating costs mainly for X-ray tubes and filters. Limited sensitivity to amorphous coatings and small (< 3 nm) particles reduces applicability to ultrasmall NPs.

1.3.3 Size Distribution and Surface Charge

Nanoparticle Tracking Analysis (NTA) NTA tracks individual particles in Brownian motion via optical microscopy, extracting size distributions and concentration [9]. Provides number-based rather than intensity-weighted distributions, but lower throughput and operator bias in threshold settings. Instruments cost approximately 80 000 €.

Zeta Potential Measurements Electrophoretic light scattering yields zeta potential, reflecting surface charge and colloidal stability [20]. Essential for predicting aggregation behavior in suspension. Instruments (around 40 000 €) require dilute suspensions and assume uniform surface potential.

1.3.4 Scanning Electron Microscopy - In Depth

SEM is one of the most versatile and widely used techniques for nanoparticle characterization, particularly for metallic systems. By rastering a focused electron beam across a sample and detecting emitted electrons, SEM provides high-resolution topographic, compositional, and crystallographic information over large fields of view [16, 28].

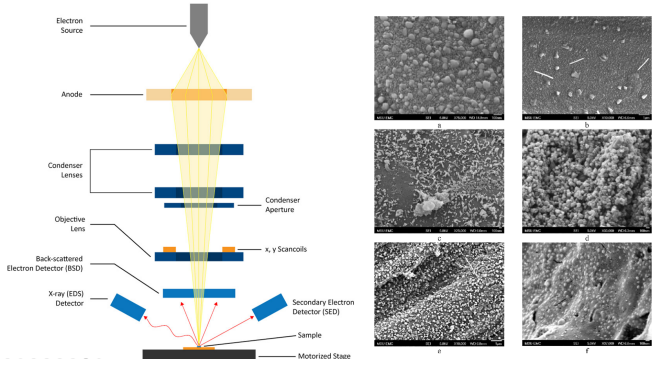

Figure 3. (left) Scanning Electron Microscope (right) SEM Image

Principle of Operation In SEM, a thermionic or field-emission electron gun provides a beam of electrons accelerated to energies between 0.5 kV–30 kV. The beam is focused by electromagnetic lenses and scanned in a raster pattern over the sample surface. Interactions between primary electrons and the specimen generate several signals:

1. Secondary electrons (SE): Low-energy (< 50 eV) electrons emitted from the top few nanometers of the surface, providing high-contrast topographic images with lateral resolution down to 1 nm [28].
2. Backscattered electrons (BSE): High-energy electrons reflected by elastic scattering; contrast scales with atomic number (Z), enabling compositional imaging of metallic nanoparticles against lower-Z substrates [16].
3. X-rays (EDS): Characteristic X-rays emitted upon electron-shell ionization; collected by an energy-dispersive spectrometer for elemental mapping [16].

Instrumentation and Detectors Modern SEMs employ a field-emission gun (FEG) for sub-nanometer probe sizes, vacuum chambers adjustable between high (< 1×10^{-6} Pa) and variable pressure (1 Pa) modes [13]. Key components include aperture and stigmator assemblies for beam shaping, objective lenses for focusing, scan coils for beam deflection, and multiple detectors:

1. Everhart–Thornley SE detector: A scintillator photomultiplier system optimized for SE collection.
2. Solid-state BSE detector: Semiconductor diode array offering faster signal and compositional contrast.
3. In-column detectors: Position below the pole piece for high-efficiency SE collection and enhanced resolution in FEG-SEMs [28].
4. EDS detector: Silicon drift detector (SDD) with energy resolution $\sim$ 130 eV, enabling rapid elemental mapping.

Capital investment for a state-of-the-art FEG-SEM with EDS and variable-pressure capability ranges from 300 000 € to 700 000 €. Annual service contracts, cryo-pumps, detectors' maintenance, and consumables (stubs, carbon/tungsten tape, conductive coatings) add approximately 25 000 € to 40 000 € to operating costs.

Sample Preparation Accurate imaging of metallic nanoparticles demands meticulous preparation:

1. Deposition: Drop-cast or spin-coat a dilute NP suspension on conductive substrates (carbon-coated stubs, silicon wafers).
2. Drying: Gentle drying under inert gas or vacuum to prevent aggregation and coffee-ring effects.
3. Coating (if needed): For non-conductive matrices or biological samples, sputter-coat with a 2 nm to 5 nm layer of gold or platinum to mitigate charging; may obscure sub-5 nm features [16].
4. **Low-vacuum/Variable-pressure mode:** For uncoated samples, operate at 10 Pa to 50 Pa water vapor or nitrogen to neutralize charge without coating [13].

Imaging Modes and Analytical Workflows Plan-view imaging is performed using standard SE imaging at 5 kV to 15 kV

to measure particle size, shape distributions, and surface assemblies. Tilted-view and stereo-pair approaches involve dual-axis tilting to reconstruct the three-dimensional morphology of anisotropic nanoparticles [28]. BSE mapping provides qualitative information on alloy composition or core–shell contrast in bimetallic NPs (e.g., Au@Ag core–shell) when operated at 20 kV to 30 kV. Finally, EDS spectral imaging entails automated mapping across regions of interest with a pixel dwell time of approximately 1 ms to quantify elemental distribution and detect trace impurities (< 0.1 wt%).

Resolution, Throughput, and Limitations Spatial resolution can reach down to 1 nm in SE mode (FEG-SEM), though beam–sample interactions (interaction volume < 50 nm at 15 kV) and coating layers may degrade true resolution [28]. Throughput is limited by typical raster scans (1024×768 pixels), which require 30 s to 120 s per frame; automated stage and gallery loading can increase sample throughput but necessitate scripting [16]. Prolonged exposure can induce carbon buildup and sintering in metallic nanoparticles; using low-kV imaging (< 5 kV) and intermittent beam blanking helps mitigate beam damage and contamination [13]. In terms of cost, although SEM operating expenses are lower than TEM, the total cost per hour of instrument time (including amortization and staffing) is approximately 50 € to 100 €, depending on regional and facility overhead [16].

2. Sensing

Nanoparticles (NPs) exhibit unique properties that make them valuable in applications ranging from sensor coatings to biochemical detection. However, characterizing NP size and distribution typically requires time-consuming and complex instrumentation.

Traditional methods such as electron microscopy (scanning or transmission) provide direct imaging of particle dimensions but involve lengthy sample preparation and analysis [26]. Other techniques like dynamic light scattering rely on Brownian motion to infer particle size distributions, yet they often demand elaborate setups and still face limitations in throughput [26, 31]. An alternative approach is to analyze NP sedimentation behavior in a fluid, since the mix of gravity and diffusion during sedimentation is influenced by particle size and density. By monitoring how NPs settle over time (their sedimentation profile), one can potentially estimate these characteristics when combined with appropriate modeling [31]. Unfortunately, many conventional characterization protocols require significant manual intervention and long wait times between fabrication and measurement steps. This creates a need for faster, analysis techniques that minimize sample usage and accelerate feedback in nanoparticle production [31].

Honrrubia et al.'s work [18] addresses that need by introducing a microwave planar resonator sensor designed to continuously monitor NP sedimentation. Microwave resonator sensors (particularly those based on split-ring resonators (SRRs) and related structures) offer a flexible, method to characterize materials through their dielectric properties [37]. The general principle is that the resonator acts as an *LC* circuit with a high Q-factor; when a material is brought into the near field of the resonator, it modifies the effective capacitance and therefore shifts the resonant frequency [37]. The magnitude of the frequency shift depends on the permittivity and volume of the material interacting with the sensor: materials with higher dielectric constant cause larger downward shifts in the resonance frequency [37]. By designing the resonator appropriately, one can target a specific frequency range and tailor the sensitivity for a given application [33]. Spiral resonator designs are especially attractive because they achieve a longer resonant path within a compact area, yielding potentially higher Q-factor and sensitivity [23]. Planar resonator sensors have already shown promise for thin-film dielectric measurements, since miniaturized resonators confine electromagnetic fields in a small volume near the sensor surface [30].

In this context, a square spiral resonator (SSR) sensor is proposed to monitor nanoparticle sedimentation profiles in real time. The idea is that as NPs dispersed in a fluid settle onto the sensor surface, they form an accumulating layer in the sensor's sensing volume (the region of the electromagnetic near-field above the resonator).

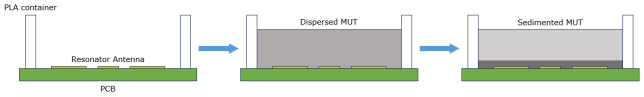

Figure 4. Diagram showing the measurement process of the MUT. First (left) the SSR and container are cleaned and all liquid and solid residues are removed, leaving the container and the PCB with the resonator antenna ready for measurement; Second (center), the dispersed MUT is poured inside the PLA container; Lastly (right), as time passes, the dispersed NPs will sediment over the PCB, leading to a measurable shift in the resonance frequency of the MUT.

This progressive deposition leads to a continuous change in the sensor's effective capacitance and hence a time-dependent shift in its resonance frequency[25]. The process is illustrated conceptually in Figure 4. Initially, the resonator is exposed to the NP dispersion (with particles distributed throughout the fluid). Over time, gravity causes NPs to migrate and concentrate near the bottom, eventually forming a uniform layer on the sensor. Once a significant layer has formed and the local NP concentration in the sensing region reaches an equilibrium, the resonance frequency stabilizes at a new value. The difference between the initial and final resonance frequencies (and the time taken to reach equilibrium) provides a "sedimentation profile" characteristic of the nanoparticle type and concentration.

The result is a sedimentation profile curve that can be analyzed to extract meaningful parameters (such as the time constant of sedimentation and the final frequency shift) which correlate with NP properties. Thus, the SSR sensor provides a novel route to rapidly characterize nanoparticles via their sedimentation dynamics, using a simple electrical measurement instead of elaborate microscopy or optical methods[19].

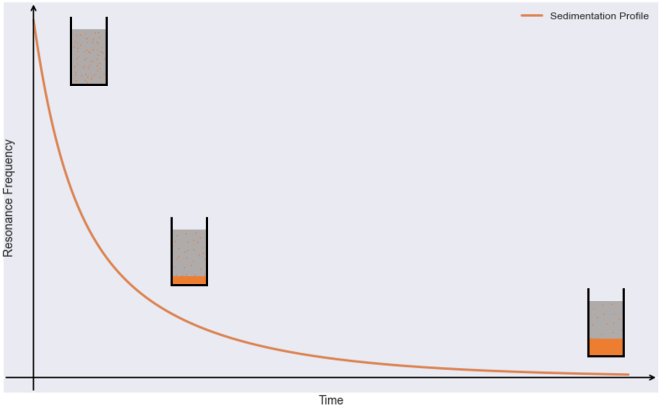

Figure 5. Conceptual diagram of the sedimentation process as sensed by the SSR sensor. Nanoparticles initially dispersed in the fluid (top) gradually settle under gravity and form a layer on the sensor surface (bottom). x-axis represents time while y-axis represent the peak of the resonance frequency measured by the VNA.

3. Measurements

Cu-NPs were synthesized using the WE method, a top-down physical fabrication technique well-suited for the production of metallic nanopowders (see Section 1.2). This method relies on the rapid vaporization of a metal conductor by the discharge of a high-voltage capacitor, leading to nanoparticle formation upon condensation in a surrounding medium.

In this study, the Cu-NPs were fabricated at the University of Pisa. The experimental setup involved cylindrical copper wires with a diameter of 1 mm and a length of 30 mm. A high-current density, ranging from 1×10^7 A m^{-2} to 1×10^9 A m^{-2}, was applied by discharging a 765 µF capacitor charged up to 10 kV. This intense current caused adiabatic heating of the wire, leading to its explosive vaporization. The vaporized copper then condensed into nanoparticles upon interaction with a surrounding medium of distilled water, which also served to contain and collect the resulting product.

The explosion process was monitored using a dedicated voltage probe (1:1000), a calibrated Rogowski coil, and a high-bandwidth oscilloscope, ensuring precise characterization of the electrical parameters during the event. The entire environment was optimized to minimize contamination: post-explosion, the vessel and electrodes were carefully cleaned with deionized water before repeating the procedure.

To ensure reproducibility and sufficient material yield, the explosion cycle was iterated ten times. The collected suspensions were subsequently subjected to a low-temperature evaporation process to isolate the dry nanopowder. The obtained Cu-NPs were then re-dispersed in deionized water, deposited onto substrates, and analysed via DLS to evaluate their size distribution and morphology.

This method offers several advantages, including the ability to produce nanoparticles without the use of chemical reagents, the rapid generation of high-purity products, and the potential to fabricate complex or multicomponent nanostructures. However, challenges such as precise control over particle size and shape, as well as the potential for oxidation, remain areas for further optimization.

Following the above-mentioned method, three samples of copper nanoparticles were created. These samples were generated using different parameters, aiming to create different sized distributions of the nanoparticles. The samples (and the names A, B, C chosen for each one) can be seen on Figure 6.

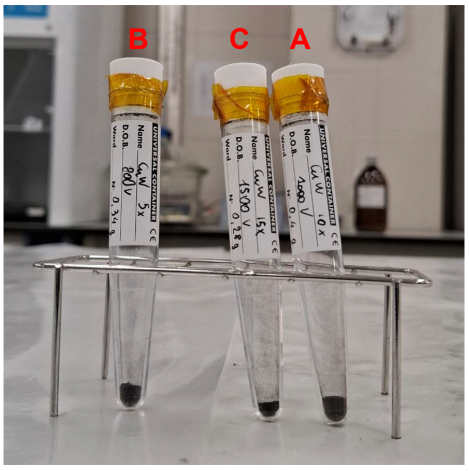

Figure 6. Three test tubes containing the three different nanoparticles, labelled A, B, C through the rest of the Thesis.

In order to measure the different sedimentation curves of the different nanoparticles, a dispersion has to be made with them. For this, pure paraffin was used as a medium in which to disperse the copper nanoparticles. The same paraffin bottle was used for all the measurements.

A concentration of 10 mg mL^{-1} was used in order to create a saturated medium in which the nanoparticles will precipitate due to gravity and sediment at the bottom of the sensor. If a non-saturated concentration was chosen, the sedimentation process would be slower and a higher percentage of nanoparticles would remain in suspension through the medium and never precipitate.

A high precision scale was used to prepare the mix of paraffin and Cu-NPs. The nanoparticles were poured in first into the test tube (and then the correct amount of paraffin was pipetted into the test tube to guarantee the desired concentration of 10 mg mL^{-1}.

The result before the sonication is that shown in the left side of Figure 7. After the process mentioned above, the result should be similar to the one shown on Figure 7 right side.

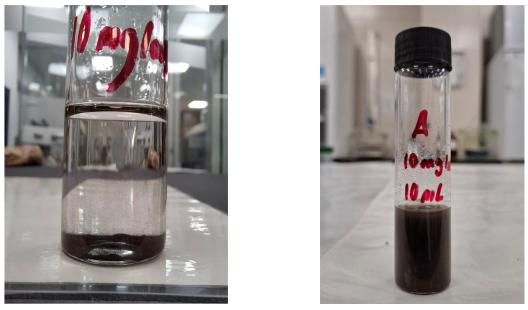

Figure 7. Before (left) and after (right) the sonication process.

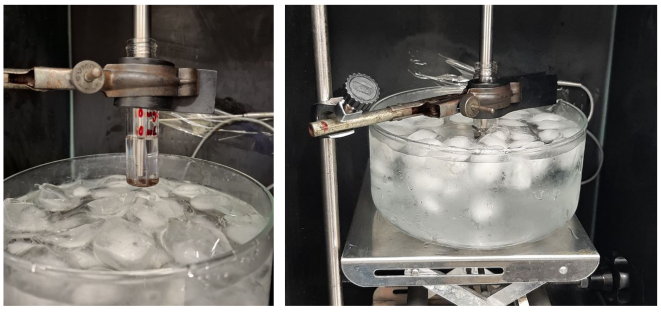

Figure 9. Test tube with nanoparticles submerged into the ice bath with the probe inside.

3.1 Sonication Time Determination

In order to determine a suitable sonication time for the dispersion and avoid sonicating for an unnecessary amount of time, an experiment was conducted. Samples of the same nanoparticle type (in this case we chose NP A, since it was the most abundant) would be sonicated for different time intervals and their sedimentation curves would be recorded and compared.

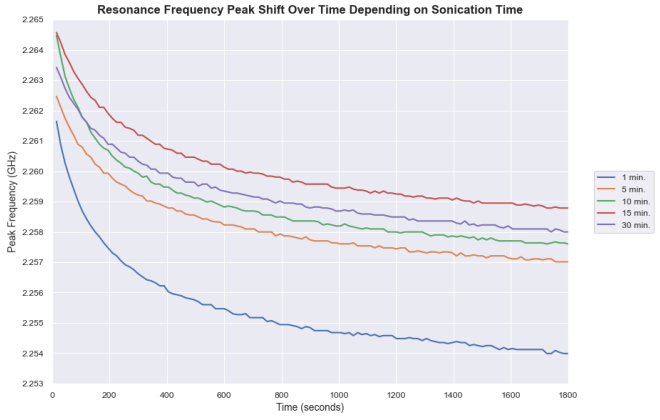

Figure 8. Sedimentation curves of the same dispersion during different sonication times.

As seen on Figure 8, the sedimentation curves keep having a slower exponential decay the longer they are sonicated until a saturation point is reached at around 15 min to 30 min. At this point, the resolution of the measurement is thee key difference since the difference between both measurements (red and purple) is only ± 1 MHz (in constrast with the 5 MHz in between the 1 min and the 15 min measurements).

With this graph, we can determine that a suitable time to sonicate the dispersion would be 15 minutes, since it grants the same results as the 30 minute one and takes half the time, allowing for faster iterations of measurements.

All of the sonications performed were done in the same conditions. The sonicated test tube would have a minimum of 5 mL and a maximum of 10 mL. The test tube would be submerged inside an ice bath with the probe tip inside the test tube just barely not touching the bottom of the test tube as seen on Figure 9.

3.2 Material Differentiation

A difference in a material's properties (permittivity, conductivity and magnetic permeability) lead to distinct shifts in a resonant sensor's response. When a planar resonator is loaded with a medium under test (MUT), its resonance frequency typically shifts downwards due to the increase in the effective permittivity.

This variation can be seen on Figure 10. The main value of interest for this research is the resonance frequency, not so much the magnitude of the peak. We can see that there is a clear distinction between some materials (for example, air and hexane), while some other materials have more similar frequencies.

It is important to note that both the Iron NPs and the Copper NPs are measurements performed in a paraffin dispersion, which is the reason their frequencies are slightly lower than that of the paraffin while still being quite close to it.

With the SSR and the VNA, the resolution of the measurements performed can perceive changes of less than 1 MHz in the resonance frequency, therefore a very viable application of this sensor is to classify different materials depending on their resonance frequency.

Apart from having different resonance frequency peaks at a certain common time after sonication, two dispersions of different material NPs will have different sedimentation curves. These curves depend on many factors, mainly the material, temperature, concentration and sonication times.

If we try and keep the changes to a minimum, we can reach some conclusions. As seen on Figure 11, even when sonicating and exposing paraffin to the same conditions as the NP dispersions, the resonance frequency does not shift significantly (the drift observed in the measurement is due to a slight temperature change in the measurement room and due to the inherent measurement error of the VNA measurement device. This error is less than 1 MHz and therefore can be ignored for our analysis.

When considering two types of metallic nanoparticles (in this case Copper and Iron), apart from a difference in any instantaneous resonance frequency peak, both sedimentation curves are different. These two NPs were fabricated following the same method, a Wire Explosion method and both are dispersions in paraffin of the same concentration. Also, it can be seen that the sedimentation process seems to follow an expo-

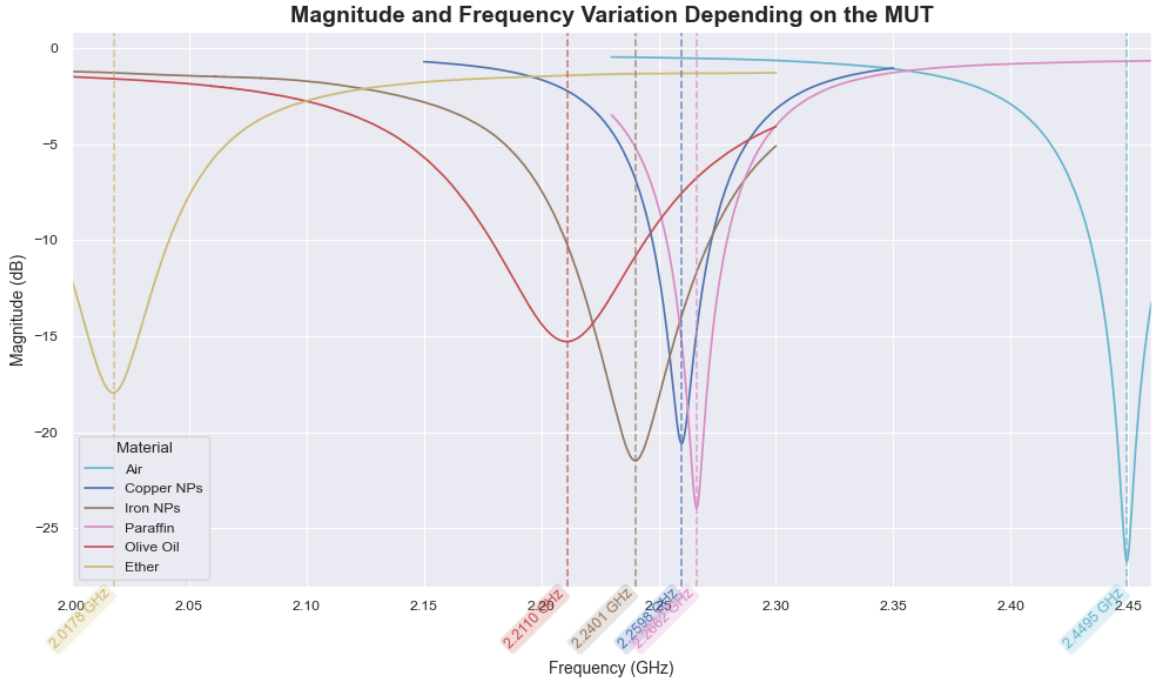

Figure 10. Resonance frequencies depending on the MUT.

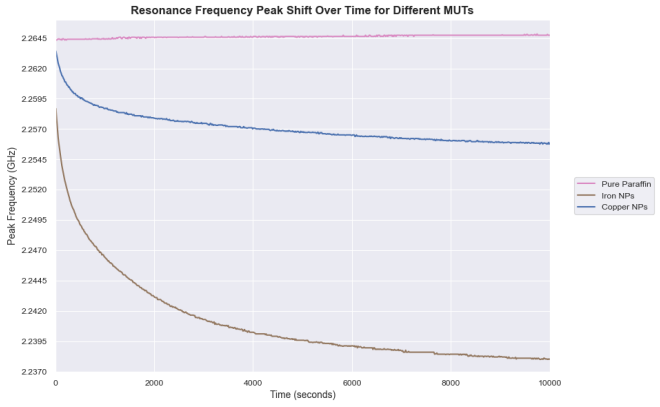

Figure 11. Resonance frequencies depending on the MUT.

nential curve. This exponential curve seems to have different time constants depending on the material. Hence, determining this time constant might prove useful for classifying the materials.

3.3 Size Differentiation

As previously mentioned, the main goal of this Thesis is to determine wether a SSR and a VNA can be used to consistently and correctly classify nanoparticles of the same material with different size distributions.

Three copper samples were provided by the University of Pisa as described in Section 3. The main intentios was to generate nanoparticles using three widely different settings during the Wire Explosion in order to try and generate three different size distributions in the nanoparticles. Once these nanoparticles were shipped to ICAI, we used the VNA alongside the SSR to measure their sedimentation curves.

Three dispersions of nanoparticles were created using a concentration of $10\,\mathrm{mg\,mL^{-1}}$. The medium in which the nanoparticles would be dispersed in is pure paraffin oil, which proves to be a non-polar liquid, cheap, and non-reactive with the nanoparticles.

The sonication times for each one of the measurements was kept constant, as well as the temperature and measurement times. Each sample was sonicated for 15 minutes in intervals of 5 s ON and 10 s OFF (leading to a total of 20 minutes for one sonication).

All nanoparticles' sedimentation times were measured multiple times in order to remove any outliers and also to take into account the variability noise inside the measurement can create.

On Figure 12, we can observe the sedimentation curves of the different nanoparticles. This graph was obtained measuring the peak resonance frequency of the nanoparticle dispersion using the VNA and the SSR mentioned in this Thesis.

As it can be observed, the curves seem quite similar, all following an exponential-like behaviour, common for sedimentation curves. The bigger nanoparticles will take less time to sediment while the smaller ones will remain a longer time suspended in the paraffin.

With this graph, a clear distinction between the nanoparticles can't be determined easily. All of the measurements seem to be very similar and, at least with a simple visual inspection, if no colors were used in the plot, it would be extremely difficult to differentiate and classify these nanoparticles.

Hence, a method to extract more information from this experiment is required. Since these signals are similar to ex-

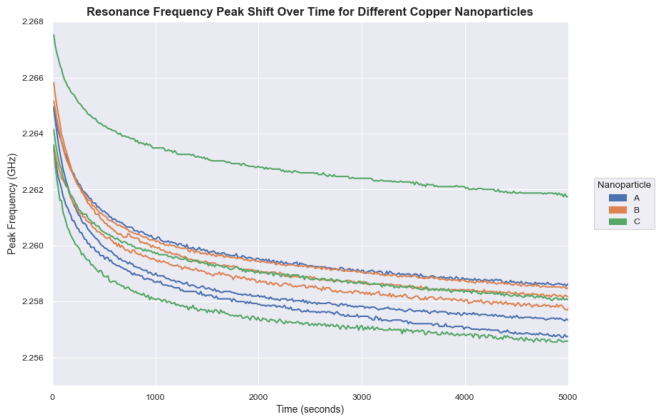

Figure 12. Peak resonance frequency over time depending on the nanoparticle sample sonicated.

ponentials, it would be interesting to obtain a time-constant distribution for each signal and see if with that information, classification would be easier.

4. Time Constant Extraction

4.1 Time Constant Extraction Procedure

Exponential decay processes are common in many areas of science and engineering. In a simple exponential decay, a quantity $m(t)$ decreases at a rate proportional to its current value. Equation 1 describes this behavior for a single decay component:

$$m(t) = f \exp\left(-\frac{t}{\tau}\right) + g \tag{1}$$

where τ is the characteristic time constant of the decay, f is the decay amplitude (initial magnitude), and g is a baseline offset [32]. Processes such as radioactive decay, population decline, certain chemical reactions, fluorescence, and magnetic resonance relaxation often follow this single-exponential model [32]. In these cases, the time constant τ (or its reciprocal, the rate constant $1/\tau$) is a key parameter that can be obtained from experimental data.

However, not all systems can be characterized by a single time constant. Many complex systems exhibit multi-exponential behavior, meaning the observed decay is a combination of multiple exponential components or even a continuous distribution of time constants. For example, the decay of magnetization in confined media (as in NMR experiments on porous materials) involves multiple decay rates, and the effective "time constant" of such a system is actually a distribution rather than a single value [34]. In these cases, using a single τ in Equation 1 is insufficient; instead, one must consider multiple exponentials contributing to $m(t)$.

4.1.1 Multi-Exponential Formulation

To model systems with more than one decay process, the single-exponential model generalizes to a sum or continuum of exponentials. In the simplest multi-exponential scenario, one might have a discrete sum of two or more exponential terms. For instance, a system with two sequential decay processes could be described (conceptually) by an expression like [32]:

$$m(t_1, t_2) = f_1 \exp\left(-\frac{t_1}{\tau_1}\right) + f_2 \exp\left(-\frac{t_2}{\tau_2}\right) + g \tag{2}$$

In equation 2, τ_1 and τ_2 are two distinct time constants for two stages of decay (with t_1 and t_2 being time variables in each stage), and this would yield a bi-exponential decay behavior. While this two-component example illustrates multiple decays, real systems can be even more complex.

In the most general case, the decay signal can be viewed as a continuous superposition of many exponential decays with different time constants. Instead of summing a few discrete terms, one can consider a distribution function $f(\tau)$ that tells us how much contribution comes from decays of characteristic time τ. Equation3 expresses the measured signal as an integral (continuous sum) of exponential decays weighted by this distribution:

$$m(t) = \int_0^\infty f(\tau) \exp\left(-\frac{t}{\tau}\right) d\tau + g\,, \tag{3}$$

where $f(\tau)$ is the *time-constant distribution* (often normalized so that its integral gives the total signal amplitude) and g is again any constant offset [34]. Equation 3 generalizes the decay model to account for an entire spectrum of time constants. In practice, g (baseline) can often be measured or assumed zero after appropriate corrections [34], so we will focus on the core integral term.

It is worth noting that the concept extends to higher dimensions as well. For processes involving two independent time variables (e.g. two-step decays or correlation experiments), one can define a two-dimensional distribution $f(\tau_1, \tau_2)$ and write a double integral analogous to Equation 3 [34]. Such formulations allow modeling of even more complex decay behaviors. For simplicity, we will continue our discussion with the one-dimensional case, as the core concepts are similar for higher dimensions.

4.1.2 Inverse Problem and Ill-Posedness

Determining the distribution $f(\tau)$ from the measured signal $m(t)$, as formulated in Equation 3, is a classic inverse problem[1]. This particular inverse problem is essentially an *inverse Laplace transform*: given the Laplace-transformed data $m(t)$, we aim to recover the original distribution function $f(\tau)$ [34].

Inverse Laplace transform problems are well-known to be severely ill-posed [34]. An ill-posed problem is one in which small errors or noise in the measured data $m(t)$ can lead to large and unstable variations in the solution $f(\tau)$, or worse, the solution may not be unique or may not exist at all in a meaningful way. In practical terms, this means that experimental imperfections or measurement noise make it very difficult to directly compute $f(\tau)$ with confidence.

This challenge arises because many different distributions of time constants can produce very similar decay curves when

integrated together. As a result, distinguishing which distribution is truly responsible for the observed signal requires very accurate data and careful analysis. Simply put, multi-exponential decay analysis is not a straightforward curve-fitting problem—it is a delicate process.

A common and practical approach is to discretize the time constants into a finite set of N_τ discrete values. Rather than evaluating an integral, the measured signal is approximated as a sum of exponential decays, each associated with a specific time constant τ_i:

$$m(t) \approx \sum_{i=1}^{N_\tau} f_i \exp\left(-\frac{t}{\tau_i}\right) , \tag{4}$$

where f_i is the weight (or amplitude) of the decay corresponding to τ_i [34]. Equation 4 serves as a numerical approximation of the continuous model in Equation 3, and it is widely used in practical data analysis.

In this discretized form, the problem becomes a system of linear equations. Let A be a matrix of size $N_t \times N_\tau$, where N_t is the number of time samples and N_τ is the number of assumed time constants. Each element of A is defined as:

$$a_{ij} = \exp\left(-\frac{t_i}{\tau_j}\right) \tag{5}$$

so that the system can be written in matrix-vector notation as:

$$A\,x \approx b \tag{6}$$

where $x = [f_1, f_2, \ldots, f_{N_\tau}]^T$ is the vector of unknown distribution weights, and $b = [m(t_1), m(t_2), \ldots, m(t_{N_t})]^T$ is the vector of measured data [8].

However, due to the nature of exponential functions, the matrix A is typically ill-conditioned or nearly singular, which again reflects the ill-posedness of the problem. Solving such a system directly often yields unstable and oscillatory solutions, especially in the presence of noise. Therefore, to obtain meaningful and interpretable results, we must apply stabilization techniques, which are discussed in the next section.

4.1.3 Regularization and Stabilization of the Solution

To reliably extract the time-constant distribution $x = \{f_i\}$ from noisy data, it is necessary to apply regularization techniques. Regularization introduces additional constraints or penalties that favor reasonable, smooth solutions for $f(\tau)$ at the expense of exactly fitting the noise.

A common approach is to solve a regularized least-squares optimization instead of a plain least-squares fit. In a regularized formulation, we seek the vector x that balances fitting the data with keeping x "well-behaved." This can be written as an optimization problem:

$$\min_{x \geq 0} \left\{ |0Ax - b|0_2^2 + \lambda^2\, \Omega(x) \right\} , \tag{7}$$

where the first term $|0Ax - b|0_2^2$ is the usual sum of squared errors (ensuring we fit the data closely), and the second term $\lambda^2\, \Omega(x)$ is a regularization penalty that discourages undesirable solutions. The parameter λ controls the trade-off between fidelity to the data and the smoothness or size of the solution. The notation $x \geq 0$ indicates that we also enforce a non-negativity constraint on the solution (since negative amplitudes f_i would be non-physical in most decay scenarios).

The choice of the penalty functional $\Omega(x)$ determines the type of regularization. A very common choice is Tikhonov regularization, which uses:

$$\Omega(x) = |0x|0_2^2 \tag{8}$$

i.e., the sum of squares of the components of x. In other words, the solution is penalized for having large overall magnitude or many large components. Using $\Omega(x) = |0x|0_2^2$ (with $x \geq 0$) in Equation 7 corresponds to a classical ridge-regression or Tikhonov approach. This tends to produce a smoother, more stable distribution $f(\tau)$ by filtering out the high-frequency oscillations that typically come from fitting noise. In practical terms, regularization filters out the effects of noise in the solution, at the cost of a slight loss in resolution (e.g., very sharp features in the true distribution might be smoothed out).

The non-negativity constraint $x \geq 0$ is also important. Since each f_i represents a contribution to the signal, it makes physical sense that f_i should be zero or positive (you cannot have a "negative" amount of signal component). Enforcing $f_i \geq 0$ further stabilizes the solution and avoids unphysical oscillations where positive and negative components cancel out. Many algorithms for this problem use *Non-Negative Least Squares (NNLS)* or similar methods to impose this constraint.

Solving the regularized problem (Equation 7) can be done efficiently. One convenient way (as implemented by the authors of the reference study) is to augment the matrix system $Ax = b$ with additional rows corresponding to the regularization term. For example, in the Tikhonov case, one can augment A with λI (and augment b with a vector of zeros), which turns the minimization of $|0Ax - b|0_2^2 + \lambda^2|0x|0_2^2$ into an equivalent extended linear least-squares problem. Standard algorithms can then solve this augmented system, yielding the regularized solution for x.

The end result is a computed distribution $f(\tau)$ that fits the experimental data within noise limits and avoids excessive oscillation or noise amplification.

4.1.4 Implementation

The methodology above might sound involved, but modern tools make it quite accessible. In fact, the authors of the study [3] have provided simple `MATLAB` and `Python` scripts to perform this multi-exponential analysis . Thanks to high-level numerical libraries, the entire inversion procedure (with regularization and constraints) can be implemented in only a few lines of code.

In order to test the performance of this tool, we generated a synthetic example by manually building an exponential signal

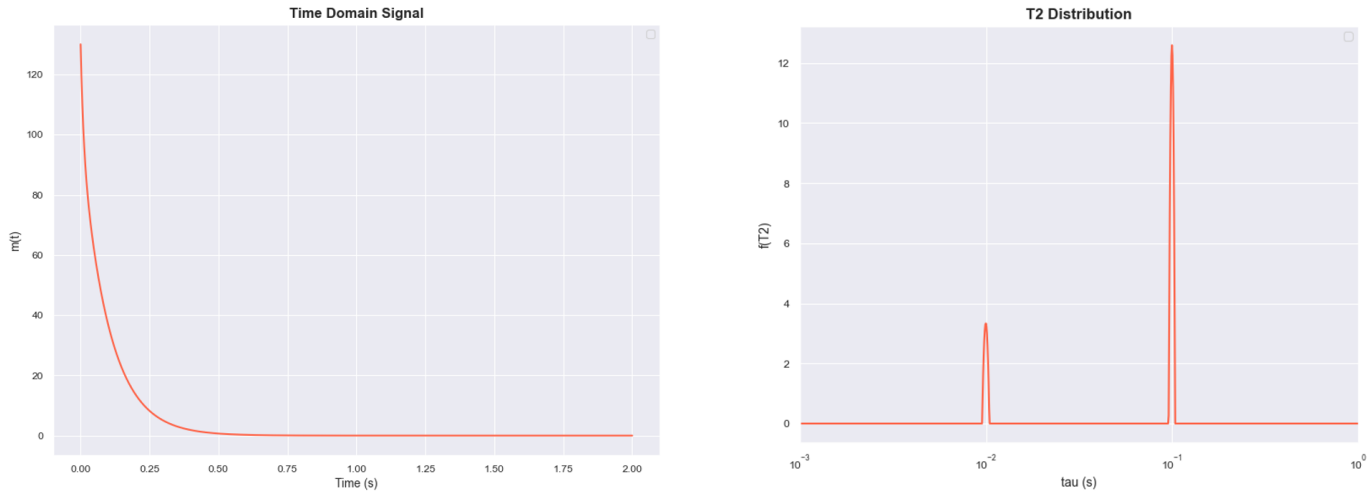

Figure 13. (left) Synthetic data generated for testing the time constant extraction; (right) results over the data.

which was the sum of two exponentials. We used Equation 9:

$$x(t) = 100e^{-10t} + 30e^{-100t} \tag{9}$$

Yielding the results shown on Figure 13.

As it can be seen on Figure 13, the time constants are perfectly determined by this method.

The output of this method is interpreted the same way as the output of a Fourier transform when talking about the sum of sinusoidal signals, but, in this case, they are exponential signals.

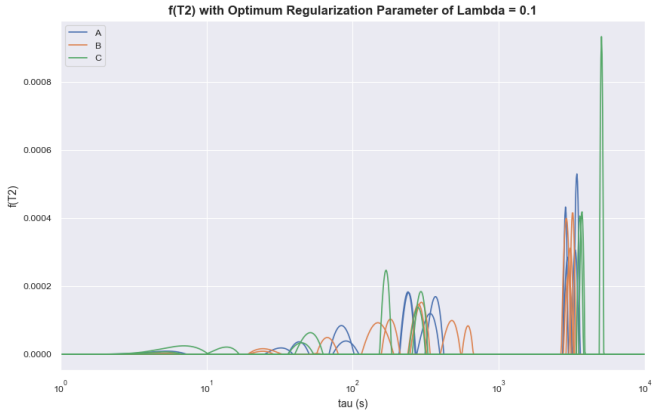

Figure 14. Time constant distribution for samples A, B and C of copper nanoparticles.

4.2 Differentiating Between Copper Nanoparticle Samples

The main goal of this Thesis is to try and differentiate in between the three Copper NP Samples fabricated at the University of Pisa. Therefore, the data in Figure 12 was input to the `Python` code and the results were recorded.

If we look at the whole time constant distribution of this dataset, we can see the results shown on Figure 14.

Looking at this, we see a wide variety of signals and the plot is quite confusing. However, we do see that the principal components are grouped in a single time constant range (between 10^3 s and 10^4 s). Therefore, we can zoom into this range, which yields the results shown on Figure 15.

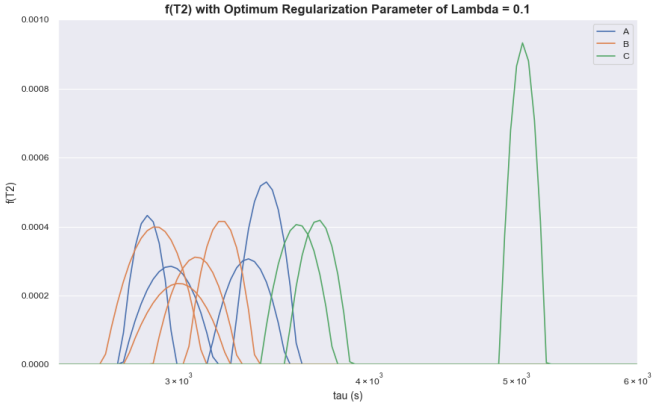

Figure 15. Time constant distribution zoomed into the principal components for samples A, B and C of copper nanoparticles.

With this new view of the results, we can clearly see two things. Firstly, nanoparticles A and B seem to be highly intertwined, with their measurements being mostly similar all the time. Secondly, nanoparticle C seems to differ more with one of the results being quite more different than the other two. This right-most result may be due to noise or even some external factors which might have affected the measruement.

Therfore, with these results, we can conclude that nanoparticles A and B will have a very similar size distribution and nanoparticle C will have a different size distribution to the one present in the other two.

4.3 Mixing Copper Nanoparticles

Since in the previous section we have determined that nanoparticles B and C are the most different, we designed a new measurement set by mixing two dispersions of nanoparticles B and C, both with the same concentration ($10\,\mathrm{mg\,mL^{-1}}$) and measuring them to compare and see if this new mix would have intermediate results to those measured in B and C.

The sedimentation curves can be seen on Figure 16.

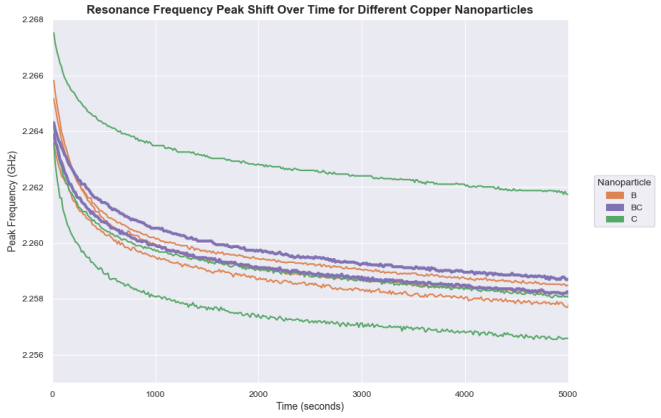

Figure 16. Sedimentation curves of copper nanoparticles B and C and the mix of BC nanoparticles.

A good sign is that these measurements are in between the values of both nanoparticles, therefore the results provided by the time constant analysis look promising.

These results can be seen on Figure 17. This figure has the same issues than the previous one, therefore, we will only focus on the principal components, which can be seen on Figure 18.

As expected the results for the BC mix of nanoparticles lay in between the results for both of the particles separetely. However, we can see that the results are very similar to those of the C nanoparticle. A simple hypothesis would be that sample C has larger nanoparticles and that when mixing nanoparticles B and C, these larger nanoparticles sediment before and therefore the B nanoparticles have a lower impact on the signal.

4.4 Differentiating Between Copper and Iron Nanoparticle Samples

Since we have been able to differentiate between nanoparticle size in the same material, the question as to wether this method can also be used to differentiate nanoparticles of different materials is only natural.

Therfore, we input the data represented in Figure 11 and compared it with the nanoparticles A B and C. The results can be seen on Figures 19 and 20 (close-up into the principal time constant).

These results show that even when not only considering the principal time constant, iron naopaprticles have a different

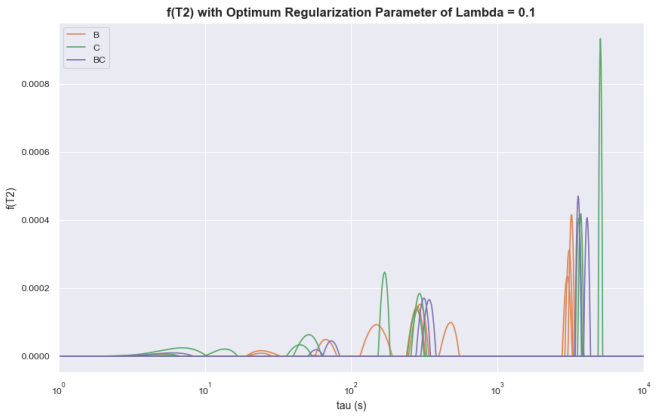

Figure 17. Time constant distribution for samples B, C and the BC mix of copper nanoparticles

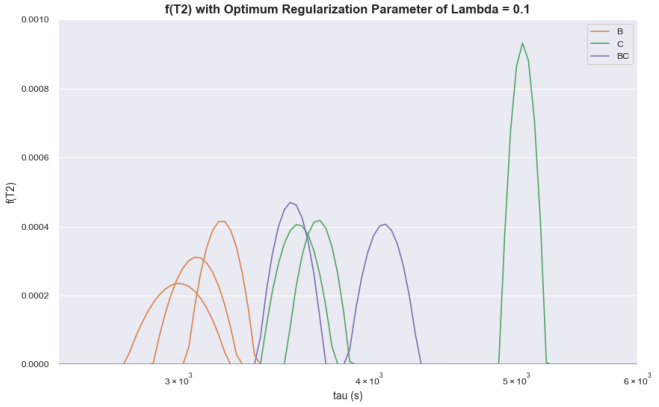

Figure 18. Time constant distribution zoomed into the principal components for samples B, C and the BC mix of copper nanoparticles.

distribution in comparison to the copper nanoparticles. Therefore, this method could potentially also be used to classify different materials.

4.5 Comparison with University of Pisa's Results

During our experiments on the nanoparticles provided by the University of Pisa, they were perfoming a characterization of the nanoparticles. This characterization was kept independant from our results, and vice-versa, so as to perform a double-blind experiment and not influence the results of both parties.

Table 1. Largest and smallest particle size depending on the sample.

NP	Large Particles Diameter (nm)	Small Particles Diameter (nm)
A	462	164
B	490	156
C	483	122

When looking at the results on Table 1, they do not seem to match those obtained by our research since they show that the nanoparticles in C have the smallest nanoparticles and do not have the largest particles. However, when looking at the results in Figure 21, we see that indeed nanoparticles A and

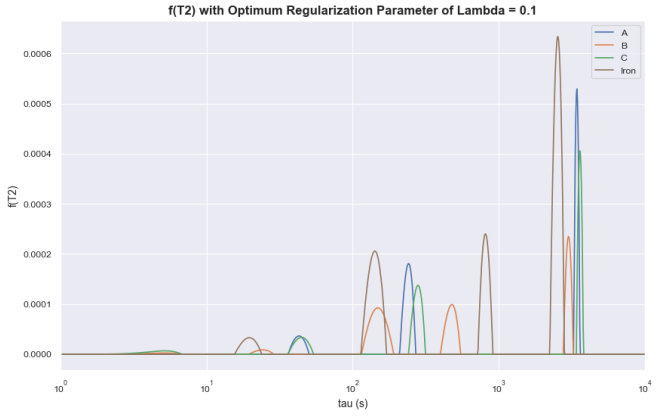

Figure 19. Time constant distribution for samples A, B and C of copper nanoparticles and one of iron nanoparticles.

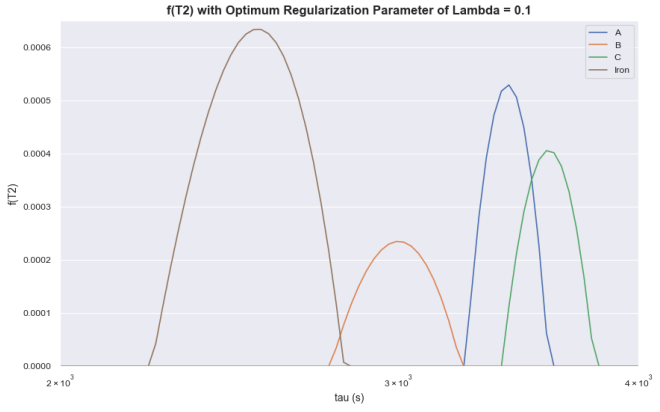

Figure 20. Time constant distribution zoomed into the principal components for samples A, B and C of copper nanoparticles and one of iron nanoparticles.

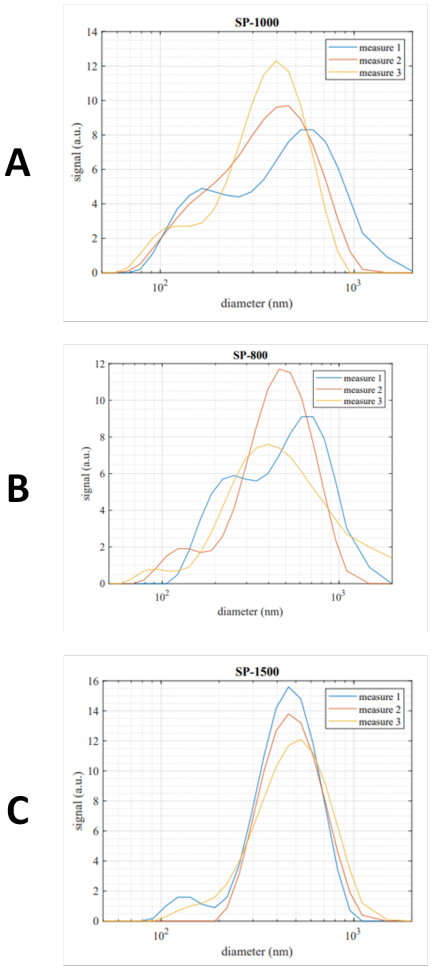

Figure 21. Data from the DLS performed by the University of Pisa on a double-blind analysis of the NPs.

B have a very similar size distribution, while C has a different size distribution.

Also, we can see that even if C does not have the largest nanoparticles, it does have more quantity of larger nanoparticles that A or B and therefore relates correctly with our results and hypotheses.

Therefore, while these two experiments were performed independently, they yield the same results. This serves as a corroboration of the results obtained in Figure 15.

5. Conclusion

5.1 Overview of the Research and Findings

This thesis has presented the design and validation of a novel sensor system for characterizing metallic nanoparticles, addressing a critical need for faster and more automated nanoparticle analysis in industrial and research settings. The proposed sensor is based on a metamaterial-inspired electromagnetic resonator (specifically, a planar square spiral resonator), which is highly sensitive to the presence and distribution of nanoparticles in its proximity.

By monitoring the real-time response of this resonator when nanoparticle dispersions are introduced, the system can profile the sedimentation of nanoparticles in a fluid and extract meaningful signatures related to their physical characteristics. This approach transforms the traditionally time-consuming task of nanoparticle characterization into an automated, real-time sensing process, aligning with modern industry demands for smart, in-line instrumentation. The research performed extensive experimental testing with metallic nanoparticle samples. Through this approach, the thesis demonstrated that the sensor can reliably capture the dynamic sedimentation curves of nanoparticle suspensions and translate them into information about particle size distribution and material composition. In essence, the work bridges the gap between advanced nanomaterials characterization techniques and practical sensing technology, providing a prototype that is both scientifically insightful and practically relevant.

5.2 Relevance to Industry 4.0 and Smart Manufacturing

A strong motivation behind this work is the growing demand for advanced sensing solutions in the context of Industry 4.0, the modern paradigm of smart manufacturing and automation.

Industry 4.0 production environments require sensors that can operate in real-time, with minimal human intervention, high precision, and reliability. Traditional nanoparticle charac-

terization methods (such as electron microscopy or laboratory particle analyzers) do not meet these criteria – they are labor-intensive, slow (often days for sample preparation and analysis, plus long waiting times for expensive equipment to be available for use), and cannot be easily integrated into an automated production line.

In contrast, the sensor developed in this thesis is inherently suited for an Industry 4.0 setting. Once deployed, it functions as a real-time monitoring device: it continuously converts the state of a nanoparticle dispersion (an external environmental condition) into an electrical signal (a resonant frequency shift or amplitude change) that can be automatically recorded and interpreted. No manual sampling and imaging are needed after the initial setup, and the measurement is non-destructive (the sample can remain in the production flow).

This means that manufacturing processes involving nanoparticles could be equipped with this kind of sensor to achieve in-line quality control and feedback. Moreover, metamaterial-based sensors like the one presented offer additional advantages that align with smart factory requirements. They are typically compact, inexpensive to fabricate (the resonator in this work is a simple printed circuit), and potentially capable of wireless or networked operation when connected to appropriate electronics. Research has shown that sensors based on metamaterials can achieve the high sensitivity and low detection limits needed in advanced industrial applications, while also being readily integrable into larger systems.

The ease of system integration is particularly important: it implies such sensors can be embedded in production equipment or pipelines without large footprints or special infrastructure.

Currently, verifying the size and consistency of manufactured nanoparticles might require taking samples to a lab and running lengthy analyses (microscopy, centrifugation, etc.), during which the production might continue unchecked or be paused. Our sensor, on the other hand, gives near-instant feedback on each batch or even continuously during production, thus avoiding the delays associated with off-line analysis. This improves throughput and can prevent batches with out-of-specification nanoparticles from going undetected until much later.

5.3 Limitations and Challenges

While the results of this thesis are promising, it is important to acknowledge the limitations and challenges of the developed sensor approach.

One fundamental limitation is that the sensor currently provides a relative or qualitative characterization rather than an absolute one. In other words, while it can tell if one sample's particles are larger on average than another's, it does not directly output the exact particle size distribution or exact material composition without reference to calibration data.

Traditional methods like electron microscopy or Dynamic Light Scattering (DLS) can give absolute measurements (e.g. an average diameter in nanometers, or a full size distribution curve).

In contrast, our resonator sensor measures an electromagnetic response that must be interpreted to infer particle properties. This interpretation typically relies on models or comparisons. For example, we might need to calibrate the sensor with known samples to create a mapping between the "time constant distribution" extracted from the sedimentation curve and actual particle size ranges. Developing a robust calibration for every new type of nanoparticle is a challenge and would be necessary before the sensor could be used as a stand-alone metrology tool.

Another challenge lies in the resolution and overlapping signatures. If two nanoparticle samples have very subtle differences in size distribution, the sensor's ability to distinguish them is constrained by signal noise and the fundamental resolution of the method. In our experiments, Samples A and B were intentionally fairly similar, and indeed the sensor correctly indicated they were alike (which is as expected). However, distinguishing subtle differences might be difficult if those differences do not produce a sufficiently different sedimentation profile within the time window of observation.

Additionally, the sensor's measurements are governed by physical contrasts (density, permittivity, magnetic permeability) between materials. If those contrasts are small, more sensitive or different resonator designs might be required.

The method's reliance on sedimentation introduces its own limitations. Sedimentation is a process that depends on gravity (or centrifugal force if aided by centrifugation), fluid viscosity, and particle density. Very small nanoparticles (say, much below 100 nm, especially if stabilized in solution) may take a very long time to sediment or might exhibit significant Brownian motion that counteracts sedimentation. In such cases, the "sedimentation profile" might be extremely slow or almost flat over practical timescales, making it hard for the sensor to get a reading within a reasonable time.

In summary, while the sensor provides rich data, making sense of that data in an automated way is non-trivial. We managed it in post-processing for the thesis, but an industrial monitor would need a reliable on-line algorithm. This could be considered a limitation of the current state of the system though it is also an opportunity for improvement.

5.4 Alignment with the Sustainable Development Goals (SDGs)

A key strength of the sensor technology developed in this thesis is its clear alignment with several United Nations Sustainable Development Goals:

- SDG 7: Affordable and Clean Energy
  Precise, real-time monitoring of metallic nanoparticles supports the reliable production of nanomaterials used in advanced catalysts, battery electrodes, and photovoltaic coatings, thereby accelerating access to clean energy technologies.
- SDG 9: Industry, Innovation and Infrastructure
  The low-cost, compact metamaterial sensor fosters resilient and sustainable industrialization by enabling inline quality control, automated process optimization, and smart factory integration without human intervention.

- SDG 12: Responsible Consumption and Production
  By shortening the feedback loop for detecting deviations in nanoparticle size and composition, the sensor minimizes waste from off-specification batches and reduces the consumption of reagents, promoting more resource-efficient manufacturing.

References

[1] Armin Afrough, Rasoul Mokhtari, and Karen L. Feilberg. "Simple MATLAB and Python scripts for multi-exponential analysis". In: *Magnetic Resonance in Chemistry* (2023).

[2] V. Amendola and M. Meneghetti. "Size evaluation of gold nanoparticles by UV–vis spectroscopy". In: *Journal of Physical Chemistry C* 111.40 (2017), pp. 15021–15024.

[3] L. Arnaut. "Reaction order and rate constants". In: *Chemical Kinetics* (2021).

[4] S. Bhattacharjee. "DLS and zeta potential – What they are and what they are not?" In: *Journal of Controlled Release* 235 (2016), pp. 337–351.

[5] Amra Bratovcic. "Diferent applications of nanomaterials and their impact onthe environment". In: *International Journal of Material Science and Engineering* (2019).

[6] B. D. Cullity and S. R. Stock. *Elements of X-ray Diffraction*. Prentice Hall, 2001.

[7] M.-C. Daniel and D. Astruc. "Gold nanoparticles: assembly, supramolecular chemistry, quantum-size-related properties, and applications toward biology, catalysis, and nanotechnology". In: *Chemical Reviews* 104.1 (2004), pp. 293–346.

[8] S. Deoni. "Biophysical and physiological principles of T1 and T2". In: *Advances in Magnetic Resonance Technology and Applications* (2020).

[9] R. A. Dragovic, C. Gardiner, and A. S. Brooks. "Sizing and phenotyping of cellular vesicles using Nanoparticle Tracking Analysis". In: *Nanomedicine* 7.6 (2011), pp. 780–788.

[10] Erik C. Dreaden et al. "The golden age: gold nanoparticles for biomedicine". In: *Chemical Society Reviews* (2012).

[11] Anu Mary Ealia and Saravanakumar. "A review on the classification, characterisation, synthesis of nanoparticles and their application". In: *IOP Conference Series: Materials Science and Engineering* (2017).

[12] László Égerházi and Tamás Szörényi. "The Potential of Wire Explosion in Nanoparticle Production inTerms of Reproducibility". In: *MDPI Materials* (June 12, 2024).

[13] R. F. Egerton. *Physical Principles of Electron Microscopy: An Introduction to TEM, SEM, and AEM*. Springer, 2005.

[14] R. F. Egerton. "Radiation Damage to Organic and Inorganic Specimens in the TEM". In: *Micron* 42.10 (2011), pp. 147–160.

[15] Hamid Reza Ghorbani. "A Review of Methods for Synthesis of Al Nanoparticles". In: *Oriental Journal of Chemistry* (Nov. 20, 2014).

[16] J. I. Goldstein, D. E. Newbury, and D. C. Joy. *Scanning Electron Microscopy and X-ray Microanalysis*. Springer, 2017.

[17] A. Henglein. "Physicochemical properties of small metal particles in solution: "Microelectrode" reactions, chemisorption, composite metal particles, and the atom-to-metal transition". In: *Journal of Physical Chemistry B* 105.48 (2001), pp. 10590–10594.

[18] Miguel Monteagudo Honrubia. "Machine Learning techniques to enhancethe capacitive sensing of microwaveresonant structures". PhD thesis. Universidad Pontifica Comillas - ICAI.

[19] Miguel Monteagudo Honrubia et al. "Measuring Sedimentation Profiles for Nanoparticle Characterization through a Square Spiral Resonator Sensor". In: *Nanomaterials in Chemical Sensors* (Apr. 2024).

[20] R. J. Hunter. "Zeta Potential in Colloid Science: Principles and Applications". In: *Academic Press* (1981).

[21] Prasad Govindrao Jamkhandea et al. "Metal nanoparticles synthesis: An overview on methods of preparation,advantages and disadvantages, and applications". In: *Journal of Drug Delivery Science and Technology* (July 23, 2019).

[22] Nadeem Joudeh and Dirk Linke. "Nanoparticle classifcation, physicochemicalproperties, characterization, and applications:a comprehensive review for biologists". In: *Journal of Nanobiotechnology* (2022).

[23] K. Kong et al. "Raman spectroscopy for medical diagnostics—From in-vitro biofluid assays to in-vivo cancer detection". In: *Advanced Drug Delivery Reviews* (2015).

[24] M.M. Modena et al. "Nanoparticle Characterization: What to Measure?" In: *Advanced Materials* (May 2019).

[25] Vicky V. Mody et al. "Introduction to metallic nanoparticles". In: *Journal of Pharmacy and Bioallied Sciences* (Dec. 2010).

[26] M. Naito et al. "Nanoparticle Technology Handbook". In: *Nanoparticle Technology Handbook, 3rd ed.* (2018).

[27] Kang Pan and Qixin Zhong. "Organic nanoparticles in foods: fabrication, characterization, and utilization." In: *Annu Rev Food Sci Technol* (2016).

[28] L. Reimer. *Scanning Electron Microscopy: Physics of Image Formation and Microanalysis*. Springer, 1998.

[29] Emil Roduner. "Size matters: why nanomaterials are different". In: *Chemical Society Reviews* ().

[30] M. Rosh Abarbanel et al. "Thermal response of CuO/polydopamine nanospheres under NIR laser irradiation". In: *Ceramics International* (2023).

[31] A. Rygula et al. "Raman spectroscopy of proteins: A review". In: *Journal of Raman Spectroscopy* (2013).

[32] Y.-Q. Song et al. "T1–T2 correlation spectra obtained using a fast two-dimensional Laplace inversion". In: *Journal of Magnetic Resonance* (2002).

[33] Z. Starowicz et al. "The tuning of the plasmon resonance of the metal nanoparticles in terms of the SERS effect". In: *Colloid and Polymer Science* (2018).

[34] H. C. Torrey. "Bloch equations with diffusion terms". In: *Physical Review* (1956).

[35] Naoki Toshima and Tetsu Yonezawa. "Bimetallic nanoparticles—novel materials for chemical and physical applications". In: *New Journal of Chemistry* (1998).

[36] D. B. Williams and C. B. Carter. *Transmission Electron Microscopy: A Textbook for Materials Science*. Springer, 2009.

[37] R. Wojnarowska et al. "Surface enhanced Raman scattering as a probe of the cholesterol oxidase enzyme". In: *Applied Physics Letters* (2015).

Acknowledgments

I want to sincerely thank my parents for their constant support over these six years. I'm also very grateful to my thesis directors, Dr. Romano Giannetti and Dr. Francisco Javier Herraiz Martínez, for their guidance and help throughout this project.